Magnetic Nanopowders: Ultrasound-Assisted Electrochemical Preparation and Properties

Jean-Luc Delplancke,*,† Jean Dille,† Jacques Reisse,‡ Gary J. Long,*,§ Amitabh Mohan,§ and Fernande Grandjean||

Materials Science and Electrochemistry Laboratory, CP 194/03, Université Libre de Bruxelles, 50 Avenue Roosevelt, B-1050 Brussels, Belgium; Organic Chemistry Laboratory, CP 165, Université Libre de Bruxelles, 50 Avenue Roosevelt, B-1050 Brussels, Belgium; Department of Chemistry, University of Missouri—Rolla, Rolla, MO 65409-0010; and Institute of Physics, B5, Université de Liège, B-4000 Sart-Tilman, Belgium

Received July 22, 1999. Revised Manuscript Received October 26, 1999

The development of cost-effective nanopowder production methods has been a major obstacle to the development and industrial utilization of nanostructured materials. This paper describes a new cost-effective production technology for these materials which combines both pulsed electrochemistry and pulsed ultrasound. This technique has been applied to the synthesis of pure and binary and ternary alloyed nanopowders containing iron, cobalt, and nickel. The resulting nanopowders have been characterized by transmission electron microscopy, X-ray fluorescence, transmission high-energy electron diffraction, X-ray diffraction, and Mössbauer spectroscopy. The results indicate that this new production method is ideal for the preparation of high performance nanocomposite powders and related high-density nanocomposite materials.

Introduction

Unique physical, chemical, mechanical, electrical, and tribological properties are often observed for fine to ultrafine particles with mean diameters in the range of 5−100 nm.[1−12] Over the past 15 years, considerable effort has been devoted to understanding the fundamental behavior of fine and ultrafine particles, clusters, and materials assembled from such particles. The unique observed properties often seem to result from the high ratio of the surface or interfacial atoms to the bulk crystalline lattice atoms.

Unfortunately, the commercial utilization of these new nanosized materials is still quite limited. According to a recent survey published by European experts in nanotechnology,[13] the absence of cost-effective nanopowder production methods is responsible for this lack of utilization. As a consequence, there has been little extension of the academic research on nanoparticles into new commercial products. In contrast, electrochemistry is a well-developed industrial technique often used to produce powders, mainly copper, iron, nickel, and cobalt powders, with a mean diameter ranging from 10 to 100 μm.[14−17] A reduction of the mean diameter of electrolytically prepared particles has been achieved recently by several methods including increased agitation of the electrolytic bath, increased plating current density, pulsed reversed current deposition, and the addition of organic electrocrystallization inhibitors.[14,15,18−21] Nanodeposits or micropowders with a mean diameter of between 1 and 10 μm, but occasionally contaminated by the electrolyte or the inhibitors, have been produced.

The purpose of this paper is to describe a new electropulse technique that combines pulsed electrodeposition and pulsed ultrasound. This technique may be used to produce uncontaminated powders with a regular

† Materials Science and Electrochemistry Laboratory, Université Libre de Bruxelles.
‡ Organic Chemistry Laboratory, Université Libre de Bruxelles.
§ University of Missouri—Rolla.
|| Université de Liège.

(1) Birringer, R. In *Nanophase Materials: Synthesis - Properties - Applications*; Hadjipanayis, G. C., Siegel, R. W., Eds.; Kluwer Academic Publishers: Dordrecht, 1994; p 157.
(2) Gleiter, H. *Prog. Mater. Sci.* **1991**, *33*, 223.
(3) Siegel, R. W. *Annu. Rev. Mater. Sci.* **1991**, *21*, 559.
(4) Gleiter, H. *Nanostruct. Mater.* **1995**, *6*, 3.
(5) Suryanarayana, C. *Int. Mater. Rev.* **1995**, *40*, 41. Suryanarayana, C.; Froes, F. H. *Metall. Trans.* **1992**, *23A*, 1071.
(6) Weissmüller, J. In *Synthesis and Processing of Nanocrystalline Powder*; Bourell, D. L., Ed.; Minerals, Metals, and Materials Society: Warrendale, 1996; p 3.
(7) Krishnan, K. M. *MRS Bull.* **1995**, *20*, 24.
(8) Kryder, M. H. *MRS Bull.* **1996**, *21*, 17.
(9) Zunger, A. *MRS Bull.* **1998**, *23*, 15.
(10) Phule, P. P.; Ginder, J. M. *MRS Bull.* **1998**, *23*, 19.
(11) Grier, D. G. *MRS Bull.* **1998**, *23*, 21.
(12) Kung, H.; Foecke, T. *MRS Bull.* **1999**, *24*, 14.
(13) Malsch, I. *Nanotechnology in Europe: Experts' Perceptions and Scientific Relations Between Sub-areas*; European Commission−JRC Institute for Prospective Technological Studies, EUR 17710 EN, ECSC-EEC-EAEC: Brussels, 1997.
(14) Ibl, N. *Advances in Electrochemistry and Electrochemical Engineering*; Wiley-Interscience: New York, 1962; Vol. 2.
(15) Calusaru, A. *Electrodeposition of Metal Powders*, Materials Science Monographs 3, Elsevier: Amsterdam, 1979.
(16) Popov, K. I.; Pavlovic, M. C. In *Modern Aspects of Electrochemistry*, White, R. E., Conway, B. E., Bockris, J. O. M., Eds.; Plenum Press: New York, 1993; Vol. 24, p 299.
(17) Mital, C. K. *J. Electrochem. Soc. India* **1973**, *22*, 251.
(18) Erb, U. *Can. Metall. Q.* **1995**, *34*, 275.
(19) Chu, C. M.; Wan, C. C. *J. Mater. Sci.* **1992**, *27*, 6700.
(20) Bagrii, V. A.; Remez, S. V.; Zhelibo, E. P.; Pavlenko, N. P. *Zh. Prikl. Khim.* **1991**, *64*, 2068.
(21) Mikhailik, O. M.; Povstugar, V. I.; Mikhailova, S. S.; Lyakhovich, A. M.; Fedorenko, O. M.; Kurbatova, G. T.; Shklovskaya, N. I.; Chuiko, A. A. *Colloids Surf.* **1991**, *52*, 324.

10.1021/cm990461n CCC: $19.00
Published on Web 03/11/2000

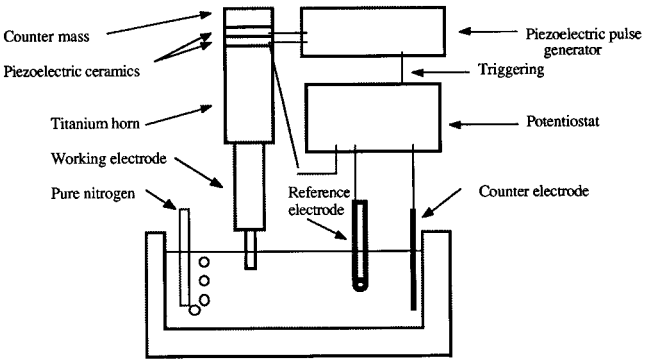

Figure 1. Schematic diagram of the ultrasound-assisted electrochemical apparatus used herein.

shape and a well-defined 10 nm to 10 μm size distribution. Pure and binary and ternary alloyed iron, cobalt, and nickel nanopowders have been obtained and are characterized herein.

Apparatus

A newly designed and locally constructed electropulse apparatus[22] is shown in Figure 1. The high-intensity ultrasound is generated by a horn which has two piezoelectric ceramic elements sandwiched between a counter mass and a titanium rod. The horn is constructed with two progressive reductions in diameter in order to achieve a final tip diameter of 10 mm. The fundamental resonance frequency of the horn is ca. 20 kHz and is measured and controlled precisely by the generator. The ultrasound intensity, typically 50 W/cm^2, is adjusted to be above the cavitation threshold of the electrolyte solution. This threshold is detected by a hydrophone (not shown in Figure 1) immersed in the electrolyte which reveals the presence of an intense half-harmonic signal that is far above the noise level.[23] At intensities above this cavitation threshold, a cloud of bubbles is clearly observed below the tip of the horn. Either a continuous or pulsed mode may be selected by the generator, but for the production of nanopowders only the pulsed mode is used. The duration of each ultrasound pulse, T_{us}, typically ranges between 100 and 1000 ms. The start of each ultrasound pulse is triggered by the potentiostat.

The titanium horn is connected to a Tacussel PRT 20−10X potentiostat. The three-electrode configuration is used to control either the anodic or cathodic potential of the tip, versus a reference electrode, or the anodic or cathodic current density passing through the tip surface. For the preparative work reported herein, the titanium horn is polarized cathodically and the anode composition corresponds to either the pure metal to be deposited on the cathode or to two or three different metals bound together with titanium wire for the deposition of the binary and ternary alloys. Dissolved oxygen is removed from the electrolyte by degassing for 1 h with pure nitrogen before each experiment. The potentiostat is used in the pulsed mode with an on time, T_{on}, ranging between 1 and 1000 ms and an off time, T_{off}, ranging between 100 and 1000 ms; see Figure 2. As shown in Figure 2, the powders are produced by out-of-phase pulses. After each electrochemical pulse, a signal is sent from the potentiostat to the generator to start the ultrasound pulse. The duration of this ultrasound pulse is shorter than the T_{off} period. During the electrochemical pulse, three-dimensional nuclei are formed on the titanium surface of the horn tip. The higher the current density or the overpotential, the smaller are the nuclei and the faster is the nucleation.[24,25] A typical diameter distribution of the copper nuclei formed during one electrochemical pulse is shown in Figure 3a. During the ultrasound pulse, the asymmetric collapse of the cavitating bubbles near the titanium surface generates shock waves and high-speed liquid jets perpendicular to the bubble surface,[26,27] jets which can have velocities greater than 100 m/s. As is shown in Figure 4, ablation of the nuclei takes place, and a cloud of nanoparticles is immediately injected into the electrolyte. As is shown in Figure 3b, a minimum nuclei diameter is required before abrasion by the mechanical effects of the ultrasound can occur. Because of the intense agitation of the electrolyte, the electrochemical double layer at the titanium surface is replenished with ions after each ultrasound pulse. The acoustic streaming produced by the ultrasound propagation and dissipation in the electrolyte, which has typical fluid velocities of between 20 and 40 cm/s, is responsible for the dispersion of the particle clouds into the electrolyte. The rest period, $T_{off} - T_{us}$, reduces this acoustic streaming and permits the production of nanopowders.

Experimental Details

The electrolyte composition is based on Aotani's bath[28] and contains 0.48 M NH_4Cl, 0.48 M H_3BO_3, 0.01 M citric acid, 0.017 M NaOH, and 0.27 M divalent metal cations as hydrated sulfates. The electrolyte pH is 3.8, and the bath temperature is maintained at 60 °C. For the deposition of pure metal powders, soluble anodes of the corresponding metal are chosen. In contrast, for the deposition of alloyed powders, an insoluble platinum anode is used. A mercury sulfate reference electrode is used, but all of the potentials given herein are referred to the normal hydrogen electrode. After 3 h of deposition, the suspensions are filtered under nitrogen with a 0.1 μm Millipore filter or a 0.01 μm Whatman filter. The powders are washed with pure ethanol and dried at room temperature. The distribution of diameters is measured by laser diffusion with a Coulter LS 130 granulometer.

Morphological studies of the powders were performed on both a JEOL JSM 820 scanning electron microscope and a Philips CM 20 scanning transmission electron microscope. For all of the alloys studied herein, the X-ray fluorescence mapping of a large sample of particle aggregates indicates compositional homogeneity; no single element particles were observed. The powder crystallinity has been analyzed by X-ray diffraction with a Siemens D5000 diffractometer and, for individual nanopowders, by high-energy electron diffraction. The bulk composition of the powders has been measured, after redissolution, with a Perkin-Elmer 2380 atomic absorption instrument. The compositions of individual particles and their homogeneity have been analyzed by X-ray fluorescence with a Philips EDAX apparatus connected to the scanning transmission electron microscope.

The magnetic properties of the iron-containing powders have been investigated by Mössbauer spectroscopy. The Mössbauer spectra were obtained at 78 and 295 K on a constant-acceleration spectrometer which utilized a room temperature rhodium matrix cobalt-57 source and was calibrated at room temperature with α-iron foil. The absorber thicknesses were ca. 50 mg/cm^2, and the resulting spectra, except for that of the pure iron sample, have been fitted with a distribution of hyperfine fields by using the method of Wivel and Morup.[29] These fits use a distribution of 22 sextets in which the areas of the components of each sextet are constrained to be in the ratio of 3:2:1:1:2:3. Thus, the only variables in these fits are the isomer shift, the quadrupole shift, the line width, and the relative contribution of each sextet. In these fits, the accuracy of the isomer shifts, quadrupole splittings, and line widths has been estimated to be ±0.005, ±0.01, and ±0.01 mm/s, respec-

(22) Winand, R.; Reisse, J.; Delplancke, J.-L. Belgian Patent 1994, no. 09400555 "Dispositif pour la production de poudres ultrafines."
(23) Leighton, T. G. *The Acoustic Bubble*; Academic Press: London, 1994.
(24) Winand, R. *Hydrometallurgy* **1992**, *29*, 567.
(25) Winand, R. *Application of Polarization Measurements in the Control of Metal Deposition*; Warren, I. H., Ed.; Elsevier: Amsterdam, 1984; p 47.
(26) Crum, L. A. *Proc. 1982 Ultrasonics Symp.* **1982**, *1*, 1.
(27) Philipp, A.; Lauterborn, W. *J. Fluid Mech.* **1998**, *361*, 75.
(28) Aotani, K. *J. Electrochem. Soc. Jpn.* **1952**, *20*, 31.
(29) Wivel, C.; Morup, S. *J. Phys. E. Sci. Instrum.* **1981**, *14*, 605.

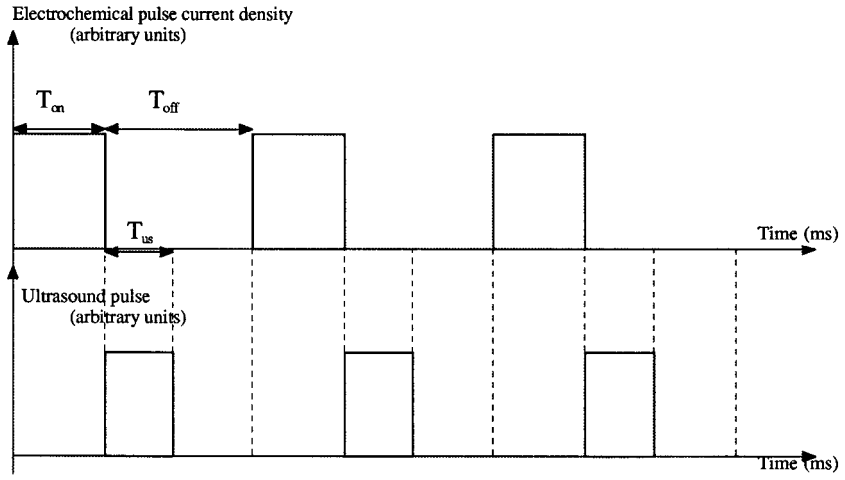

Figure 2. Out-of-phase electrochemical and ultrasound pulses.

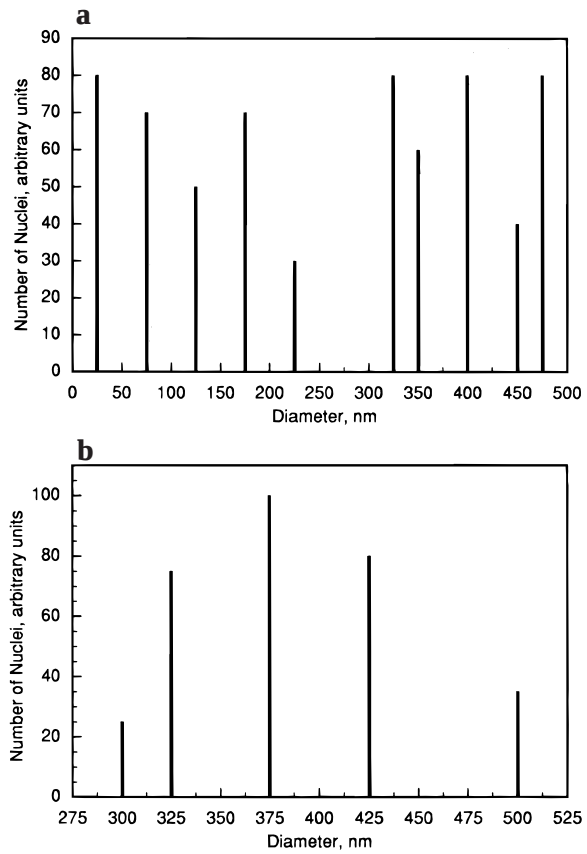

Figure 3. (a) Diameter distributions of the nuclei formed after each electrochemical pulse. (b) Diameter distribution of the nanopowders collected after 15 min.

tively. The accuracy of the average hyperfine fields has been estimated to be ±3 kOe. In contrast, because the spectra of the iron sample also contain two intense paramagnetic quadrupole doublets, they have been fitted with discrete sextets and doublets, and the estimated accuracy is probably better than the values listed above. The line widths of the six components of the discrete sextets used were constrained to be in the ratio $\Gamma + \Delta\Gamma:\Gamma + 0.5\Delta\Gamma:\Gamma:\Gamma + 0.5\Delta\Gamma:\Gamma + \Delta\Gamma$.

Results and Discussion

Pure Metals. Of the three metals under study, the most noble is nickel and the least noble is iron. Pure metal particles were produced[30] at a constant current density of 2000 A/m^2 with a T_{on} of 600 ms, a T_{off} of 400 ms, and a T_{us} of 300 ms. The deposition current yield is 60% and, as is shown in Figure 5a for nickel, the mean diameter is typically 50 nm. The hydrogen evolution which takes place during electrolysis keeps the redox potential of the electrolyte at a low value, thus preventing further dissolution of the nanopowders into the electrolyte. Nevertheless for iron, redissolution of the nanoaggregates is observed. During filtration under nitrogen, a slight oxidation of the iron particles occurs. This oxidation is not observed for the nickel or cobalt nanopowders.

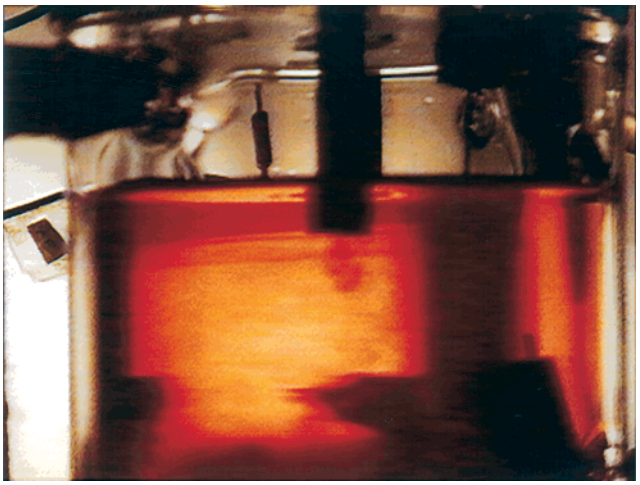

Figure 4. High-speed camera picture of the particle cloud sent into the electrolyte during each ultrasound pulse.

An X-ray fluorescence analysis reveals a slight contamination from the chloride and sulfate ions in the electrolyte. No titanium from the horn is detected in the powders. The X-ray and electron diffraction results reveal the production of face-centered cubic (fcc) nickel (see Figure 5b), hexagonal cobalt, and body-centered cubic (bcc) iron. The high pressures and high temperatures associated with the "hot spot" theory for bubble cavitation[23,31,32] do not seem to modify the crystallographic structure of the nanopowders.

(30) Delplancke, J.-L.; Di Bella, V.; Reisse, J.; Winand, R. *Mater. Res. Soc. Symp. Proc.* **1995**, *372*, 75.
(31) Suslick, K. S.; Choe, S. B.; Cichowlas, A. A.; Grinstaff, M. W. *Nature* **1991**, *353*, 414.
(32) Doktycz, S. J.; Suslick, K. S. *Science* **1990**, *247*, 1067.

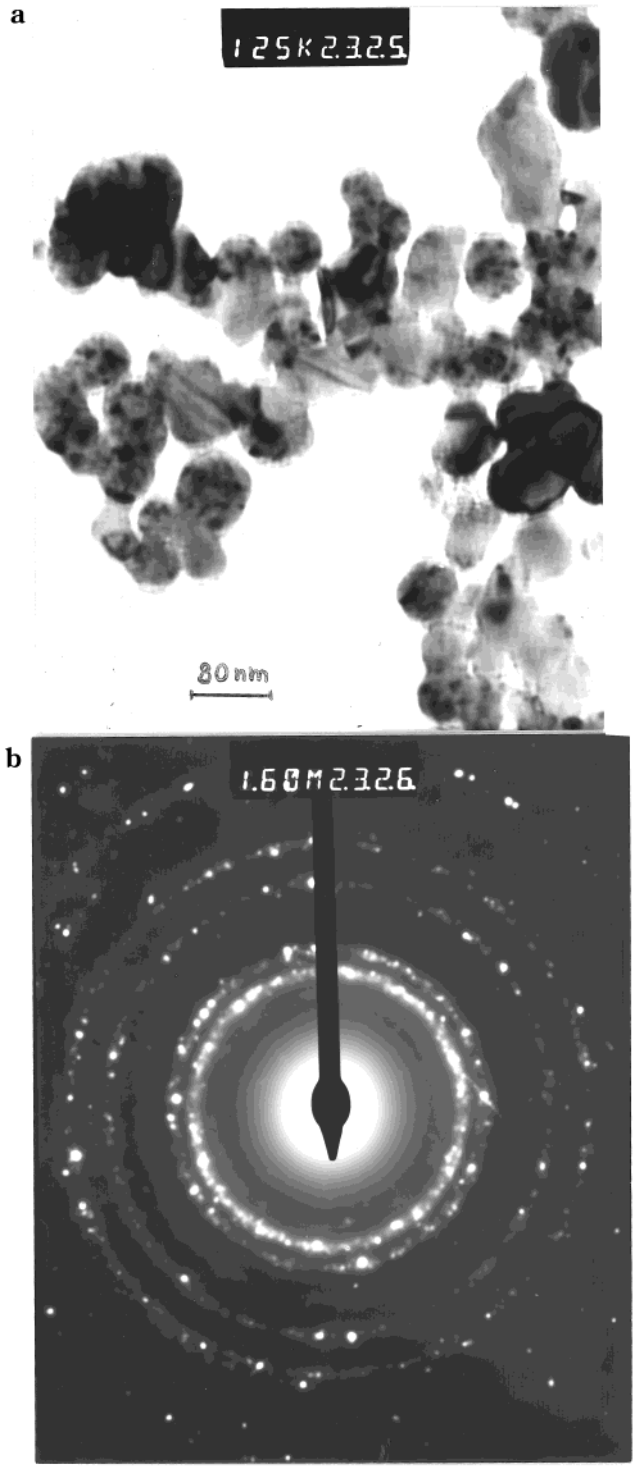

Figure 5. (a) Transmission electron microscopy photograph of the pure nickel nanopowders obtained with $J = 2000$ A/m^2, $T_{on} = 600$ ms, $T_{off} = 400$ ms, and $T_{us} = 300$ ms. (b) High-energy electron diffraction pattern of the nickel nanopowders shown in part a.

The Mössbauer spectra obtained for the powder containing only iron are unique in this study in that they show, in addition to a magnetically ordered α-iron sextet, two paramagnetic quadrupole doublets. The hyperfine parameters corresponding to the fits shown in Figure 6 are given in Table 1. The hyperfine parameters of the doublets clearly indicate that these doublets correspond to high-spin iron(II)- and iron(III)-containing complexes resulting from a reaction with the electrolyte. It is difficult to be more specific about the exact nature of these paramagnetic components, but it is clear that the hyperfine parameters do not correspond exactly to the simple hydrates of iron(II) sulfate,[33] i.e., $FeSO_4 \cdot 5H_2O$ or $FeSO_4 \cdot 7H_2O$, nor to that of anhydrous iron(III) sulfate,[34] $Fe_2(SO_4)_3$, nor to the simple hydrates of iron(II) and iron(III) chloride.[35,36] Perhaps this is not too unexpected as any such salts would be expected to be removed during the washing of the final powder. In contrast, it is quite possible that these doublets may correspond to iron(II) and iron(III) borate complexes[35,36] which could well be retained during sample washing.

At 295 K, the parameters for the major magnetic component are essentially those expected of α-iron, but at 78 K, the hyperfine field is somewhat larger than that expected for pure α-iron, an increase that is consistent with the increase observed[37,38] at 77 K for nanosized particles of α-iron and attributed to interfacial iron atoms. In addition to the α-iron-like phase, at 78 K there is also a weak magnetic component corresponding to a poorly defined iron(III) oxide, a component that is probably present at 295 K but is so broad and weak that its presence is not obvious. This component may not be intrinsic to the material but may result from exposure of the material to traces of oxygen during the powder preparation or during the measurement of the spectrum.

Binary Alloys. All of the A−B binary alloys were deposited galvanostatically at 8000 A/m^2 with a T_{on} of 300 ms, a T_{off} of 300 ms, and a T_{us} of 200 ms. Particles with a mean diameter of ca. 100 nm were produced. Five electrolyte compositions were selected for each binary system: 90 atom % A/10 atom % B; 75 atom % A/25 atom % B; 50 atom % A/50 atom % B; 25 atom % A/75 atom % B; and 10 atom % A/90 atom % B. Table 2 summarizes the composition of the electrodeposition baths, the deposited powders (as determined by bulk atomic absorption analyses), and individual particles (as determined by X-ray fluorescence on selected crystals of the binary alloys). The agreement between the compositions of the bulk powders and the individual particles is remarkable. This is an indication of the extensive homogeneity of these powders. With the exceptions mentioned below, the nanopowders have, within experimental error, the same compositions as those of the electrolytes.

For the Co−Ni binary alloys, only the composition of the highest content nickel alloys differ from that of the electrolyte. In this case, anomalous co-deposition, i.e., the preferential deposition of the less noble cobalt, is observed. This phenomenon is well-known in the electrodeposition of Co−Ni alloys.[39]

(33) Cheetham, A. K.; Cole, A. J.; Long, G. J. *Inorg. Chem.* **1981**, *20*, 2747.
(34) Long, G. J.; Longworth, G.; Battle, P.; Cheetham, A. K.; Thundathil, R. V.; Beveridge, D. *Inorg. Chem.* **1981**, *20*, 2747.
(35) Reiff, W. M.; Long, G. J. In *Mössbauer Spectroscopy Applied to Inorganic Chemistry*; Long, G. J., Ed.; Plenum Press: New York, 1984; Vol. 1, p 245.
(36) Long, G. J. In *Mössbauer Spectroscopy*; Dickson, D. P. E., Berry, F. J., Eds.; Cambridge University Press: Cambridge, 1986; p 70.
(37) Herr, U.; Jing, J.; Birringer, R.; Gonser, U.; Gleiter, H. *Appl. Phys. Lett.* **1987**, *50*, 472.
(38) Campbell, S. J.; Gleiter, H. In *Mössbauer Spectroscopy Applied to Magnetism and Materials Science*; Long, G. J., Grandjean, F., Eds.; Plenum Press: New York, 1993; Vol. 1, p 241.
(39) Brenner, A. *Electrodeposition of Alloys: Principles and Practices*; Academic Press: New York, 1963.

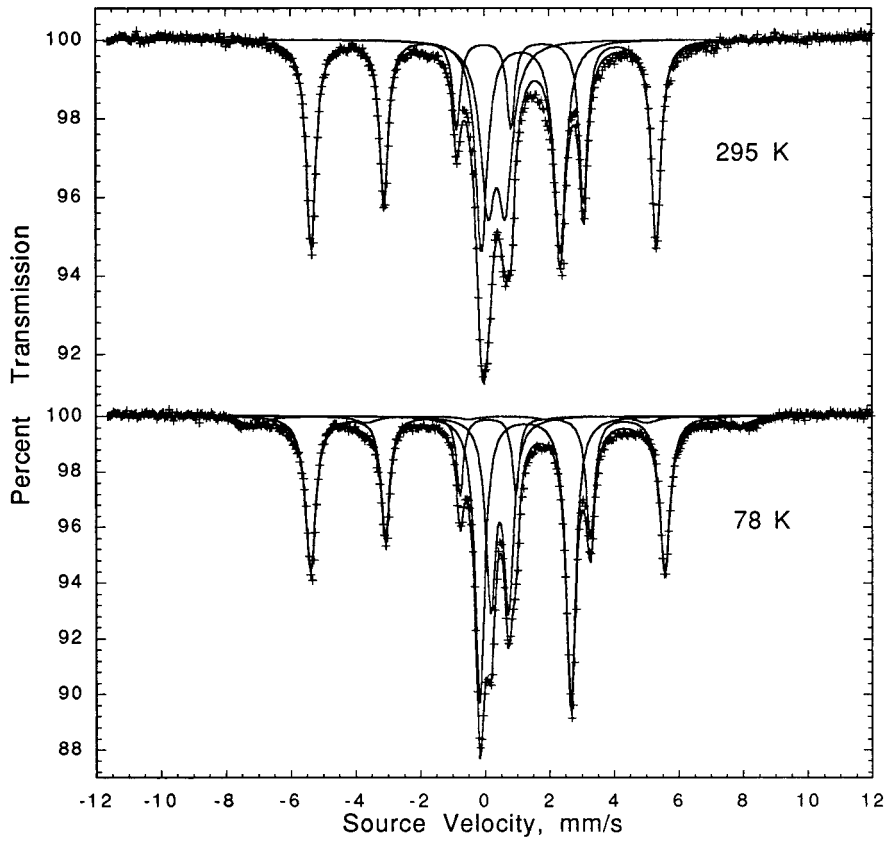

Figure 6. Mössbauer spectra of the iron sample obtained at 78 and 295 K.

Table 1. Mössbauer Spectral Parameters for the Iron Sample

T (K)	H (kOe)	δ^a (mm/s)	ΔE_Q (mm/s)	Γ (mm/s)	$\Delta\Gamma$ (mm/s)	% area
295	331	0.001	0.00[b]	0.28	0.08	46
	0	1.144	2.43	0.44		29
	0	0.395	0.54	0.53		25
78	465	0.533	−0.32[b]	0.90	0.00	6
	340	0.111	0.00[b]	0.25	0.13	39
	0	1.267	2.82	0.35		33
	0	0.469	0.56	0.36		22

[a] The isomer shifts are reported relative to room temperature α-iron foil. [b] The quadrupole shift for the magnetic spectra.

As is indicated by the thermodynamic Co−Ni phase diagram,[40] fcc cobalt and fcc nickel form a solid solution over the entire range of compositions for temperatures above 422 °C. Moreover, within the error limits, the positions of the X-ray diffraction peaks of fcc nickel correspond to those of the fcc cobalt diffracting planes. For electrolyte concentrations above or equal to 45 atom % Ni, only the diffraction pattern of fcc nickel is observed; see Figure 7. For electrolyte compositions below 50 atom % Ni, the nickel X-ray diffraction peaks are superimposed upon some peaks characteristic of hexagonal close-packed (hcp) cobalt. Electron diffraction patterns of selected binary particles reveal, independently of the concentration, only the fcc pattern and symmetry. It thus seems reasonable to assume that, independent of the electrolyte concentration, only the high-temperature stable fcc solid-solution binary particles are produced by the electropulse technique. For high cobalt concentrations in the electrolyte, these binary particles are mixed with pure hcp cobalt particles.

Table 2. Comparison of the Initial Electrolyte Bath, the Bulk, and the Individual Particle Compositions (atom %) for the Binary Alloys

electrolyte comp.		bulk comp.[a]		particle comp.[b]	
Co	Ni	Co	Ni	Co	Ni
90	10	90	10	88	12
75	25	78	22	76	24
50	50	55	45	54	46
25	75	30	70	29	71
10	90	21	79	18	82
Fe	Ni	Fe	Ni	Fe	Ni
90	10	80	20	83	17
75	25	73	27	76	24
50	50	57	43	63	37
25	75	34	66	39	61
10	90	18	82	23	77
Fe	Co	Fe	Co	Fe	Co
90	10	88	12	89	11
75	25	76	24	78	22
50	50	42	58	43	57
25	75	30	70	34	66
10	90	15	85	20	81

[a] The bulk composition, with an error of ±1 atom % for the Co−Ni and Fe−Ni alloys and ±2 atom % for the Fe−Co alloys, as determined by atomic absorption. [b] The individual particle composition, with an error of ±5 atom %, as determined by X-ray fluorescence.

For the Fe−Ni binary alloys, the agreement between the compositions of the bulk powders and the individual particles is excellent. Once again, in agreement with the X-ray fluorescence mapping, this is an indication of the excellent homogeneity of these alloys. Anomalous co-

(40) Hansen, M. *Constitution of Binary Alloys*; McGraw-Hill: New York, 1958; p 472−678.

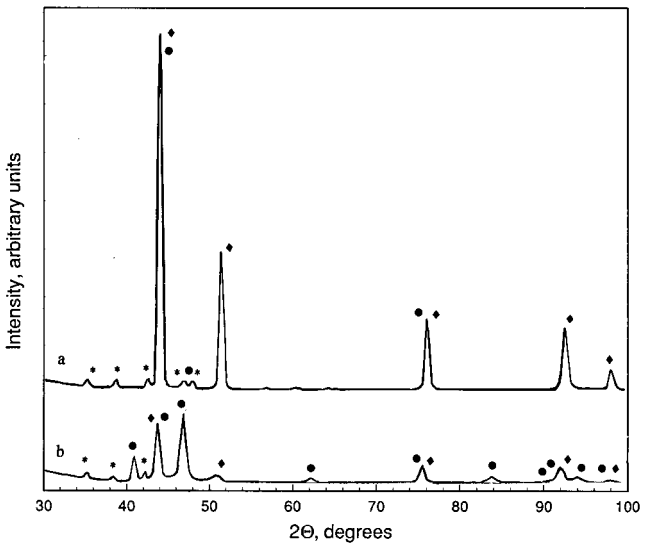

Figure 7. Pattern a: X-ray powder diffraction patterns of the $Co_{55}Ni_{45}$, $Co_{30}Ni_{70}$, or $Co_{21}Ni_{79}$ nanopowders. Pattern b: $Co_{90}Ni_{10}$ or $Co_{78}Ni_{22}$ nanopowders. Symbols: *, substrate peaks; ◆, fcc Ni (JCPDS #4-850) or fcc Co (JCPDS # 15−806) peaks; and ●, hcp Co (JCPDS #5-727) peaks.

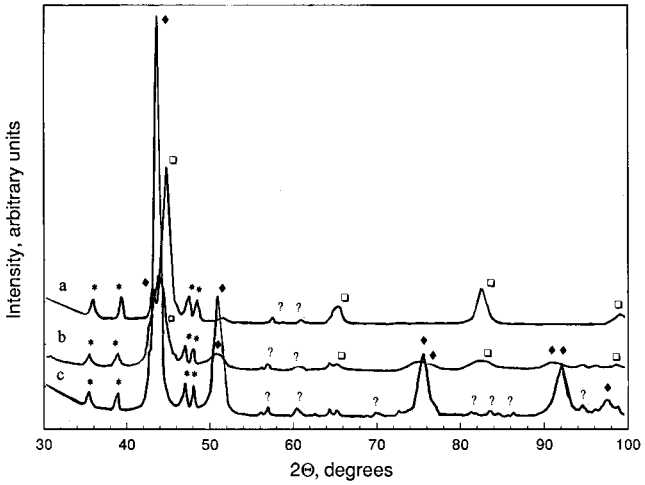

Figure 8. Pattern a: X-ray diffraction patterns of the $Fe_{80}Ni_{20}$ and $Fe_{73}Ni_{27}$ nanopowders. Pattern b: $Fe_{57}Ni_{43}$ nanopowder. Pattern c: $Fe_{34}Ni_{66}$ and $Fe_{18}Ni_{82}$ nanopowders. Symbols: *, substrate peaks; ◆, fcc Ni (JCPDS #4−850); □, bcc Fe (JCPDS #6-696) peaks; and ?, unassigned peaks.

deposition, i.e., the preferential deposition of the less noble iron, is observed except in the case of the highest iron electrolyte concentration. This phenomenon has already been observed for the electrodeposition of Fe−Ni alloys.[39]

As is indicated by the thermodynamic Fe−Ni phase diagram,[40] fcc iron and fcc nickel form a solid solution over the entire range of compositions for temperatures above 912 °C. At lower temperatures, bcc iron solid solutions, Fe_3Ni, FeNi, and $FeNi_3$, as well as fcc nickel solid solutions, are thermodynamically stable. For the two highest concentrations of iron, X-ray and electron diffraction patterns corresponding to bcc iron are observed; see Figure 8. In contrast, the patterns observed with the two highest concentrations of nickel correspond to a distorted fcc nickel alloy. A mixture of two alloy phases, one bcc phase and one fcc phase, but not pure bcc iron or pure fcc nickel, is observed for the 50/50 electrolyte composition. Accordingly, it appears that

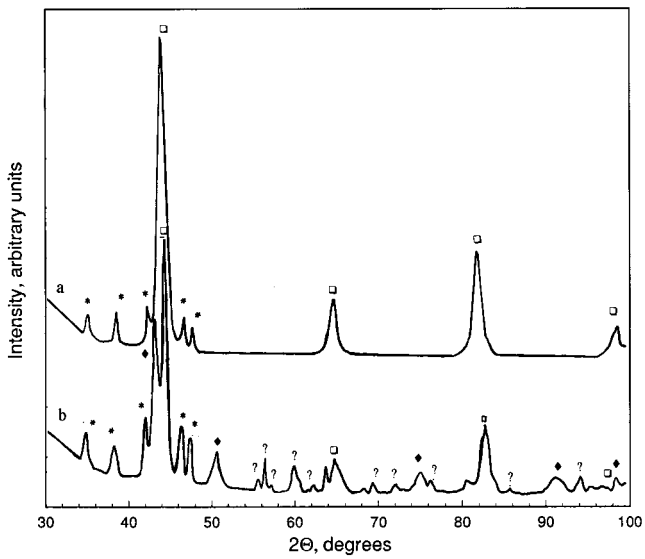

Figure 9. Pattern a: X-ray diffraction patterns of the $Fe_{88}Co_{12}$ or $Fe_{76}Ni_{24}$ nanopowders. Pattern b: $Fe_{42}Co_{58}$, $Fe_{30}Co_{70}$, or $Fe_{15}Co_{85}$ nanopowders. Symbols: *, substrate peaks; ◆, fcc Co (JCPDS # 15−806); □, bcc Fe (JCPDS #6-696) peaks; and ?, unassigned peaks.

solid solutions with ranges of compositions larger than the thermodynamic ranges are produced by the ultrasound-assisted electrochemical technique.

Again, for the Fe−Co binary alloys the agreement between the compositions of the bulk powders and the individual particles is remarkable and is an indication of the excellent homogeneity of these powders. Anomalous co-deposition, i.e., the preferential deposition of the less noble iron, is observed at the low iron electrolyte concentrations. This phenomenon is well-known in electrodeposition of Fe−Co alloys.[39] In contrast, for an iron concentration in the electrolyte above 50 atom %, the powder compositions correspond exactly to the electrolyte compositions.

As is indicated by the Fe−Co phase diagram,[40] fcc cobalt and fcc iron form solid solutions over the entire range of compositions for temperatures above ca. 1000 °C. At lower temperatures, the bcc phase is thermodynamically more stable. At high iron concentrations in the electrolyte, the nanopowders yield X-ray and electron diffraction patterns corresponding to bcc iron, in agreement with the phase diagram; see Figure 9. For electrolyte concentrations of 50 atom % cobalt, new peaks corresponding to fcc cobalt are observed superimposed upon the bcc iron pattern together with unidentified small peaks. Electron diffraction patterns on selected aggregates could not distinguish between these two phases.

Ternary Alloys. The same experimental conditions were selected for the galvanostatic deposition of the ternary alloys as was used for the binary alloys, and again particles with mean diameters of ca. 100 nm were obtained; see Figure 10. Table 3 summarizes the composition of the electrodeposition bath, the deposited powder (as determined by bulk atomic absorption analysis) and individual particles (as determined by X-ray fluorescence on selected crystals). The agreement between the averaged analysis and the local analysis of selected crystals is remarkable. The powders are

Figure 10. Transmission electron microscopy photograph of a ternary alloy nanopowder obtained with an electrolyte composition of 30 atom % Fe, 30 atom % Co, 40 atom % Ni and with $J = 8000$ A/m^2, $T_{on} = 300$ ms, $T_{off} = 300$ ms, and $T_{us} = 200$ ms.

Table 3. Comparison of the Initial Electrolyte Bath, the Bulk, and the Individual Particle Compositions (atom %) for the Fe−Co−Ni Alloys

electrolyte comp.			bulk comp.[a]			particle comp.[b]		
Fe	Co	Ni	Fe	Co	Ni	Fe	Co	Ni
10	80	10	16	76	8	17	74	8
10	10	80	17	18	66	18	15	68
80	10	10	72	18	10	75	14	12
20	60	20	25	61	14	26	58	15
20	20	60	26	27	46	28	25	48
60	20	20	59	23	19	59	22	19
30	30	40	33	32	35	34	33	33

[a] The bulk composition, with an error of ±2 atom %, as determined by atomic absorption. [b] The individual particle composition, with an error of ±5 atom %, as determined by X-ray fluorescence.

homogeneous, as confirmed by elemental X-ray fluorescence mapping of aggregate particles.

The concentration of the most noble metal, nickel, in the nanopowders is always less than that of the starting electrolyte concentration. Anomalous co-deposition takes place, especially for iron. For electrolyte concentrations above 60 atom % nickel (see Figure 11a), the X-ray diffraction patterns correspond to fcc nickel. For electrolyte concentrations above 60 atom % iron (see Figure 11b), the bcc iron pattern is observed. For electrolyte concentrations above 60 atom % cobalt (see Figure 11c), the X-ray diffraction patterns correspond to a mixture of the two above-mentioned patterns if one takes into account the superimposition of the peaks corresponding to fcc nickel and fcc cobalt.

Unfortunately, the thermodynamic phase diagrams of the ternary Fe−Co−Ni alloys are rare.[41−44] Nevertheless, our results are in agreement with the partial diagram proposed by Osaka et al.[43] which reveals an fcc phase at high nickel concentrations and a bcc phase at high iron concentrations. For the $Fe_{33}Co_{32}Ni_{35}$ nanopowders and more generally for $A_{40}B_{30}C_{30}$ alloys, only electron diffraction patterns are obtained, patterns which correspond to a pure fcc nickel or a pure fcc cobalt phase.

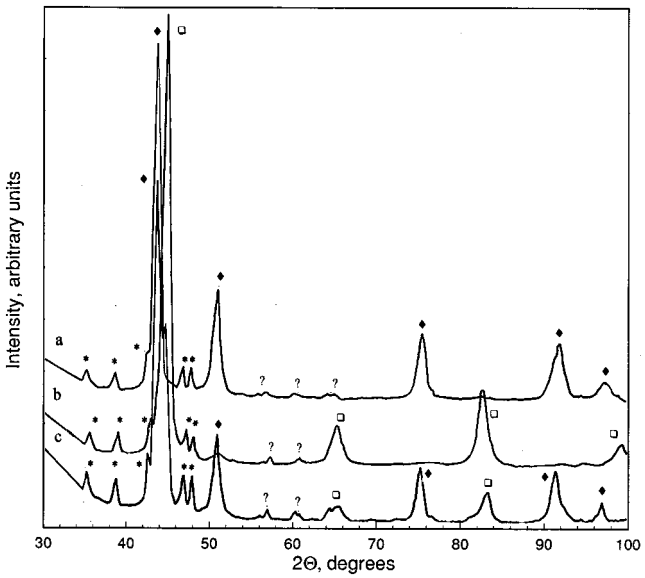

Figure 11. Pattern a: X-ray diffraction patterns of the $Fe_{17}Co_{18}Ni_{66}$ or $Fe_{26}Co_{27}Ni_{46}$ nanopowders. Pattern b: $Fe_{72}Co_{18}Ni_{10}$ or $Fe_{59}Co_{23}Ni_{19}$ nanopowders. Pattern c: $Fe_{16}Co_{76}Ni_8$ or $Fe_{25}Co_{61}Ni_{14}$ nanopowders. Symbols: *, substrate peaks; ◆, the fcc Ni (JCPDS #4-850) or fcc Co (JCPDS # 15−806); □, bcc Fe (JCPDS #6-696) peaks; and ?, unassigned peaks.

Mössbauer Spectral Analysis. Some binary and ternary alloy compositions were selected for iron-57 Mössbauer spectral analysis. It has been possible to fit these magnetic spectra with a distribution of hyperfine fields ranging from 250 to 400 kOe at 295 K and from 300 to 400 kOe at 78 K. The results of these fits for the 78 K spectra are shown in Figure 12, and the corresponding distributions[29] of the hyperfine fields are shown in Figure 13. Very similar plots are obtained for the 295 K spectra, and the hyperfine parameters resulting from the distribution fits at 78 and 295 K are given in Table 4, which also includes the results for pure iron for comparison. With the exception of $Fe_{33}Co_{32}Ni_{35}$, all of the alloys show a small paramagnetic component at ca. 0.0 mm/s with a relative area of between 2 and 4% of the total absorption area. It should be noted that, as shown in parts B and D of Figure 12, in no case was this small paramagnetic component included in the distribution fits.

The distribution method of Wivel and Morup[29] does not account for any correlation between the hyperfine parameters, and as a consequence, all such distribution fits will be symmetric. This seems to be a very good approximation for all of the spectra shown in Figure 12 except for $Fe_{57}Ni_{43}$, part B, for which there appears to be a small correlation between the hyperfine field and

(41) Raghavan, V. *J. Phase Equil.* **1994**, *15*, 526.
(42) Rivlin, V. G. *Int. Met. Rev.* **1981**, *5*, 269.
(43) Osaka, T.; Takai, M.; Hayashi, K.; Ohashi, K.; Saito, M.; Yamada, K. *Nature* **1998**, *392*, 796.
(44) Goman'kov, V. I.; Puzei, I. M.; Maltsev, Y. I.; Pedrenko, E. D. *Fiz. Metal. Metalloved* **1970**, *29*, 429.

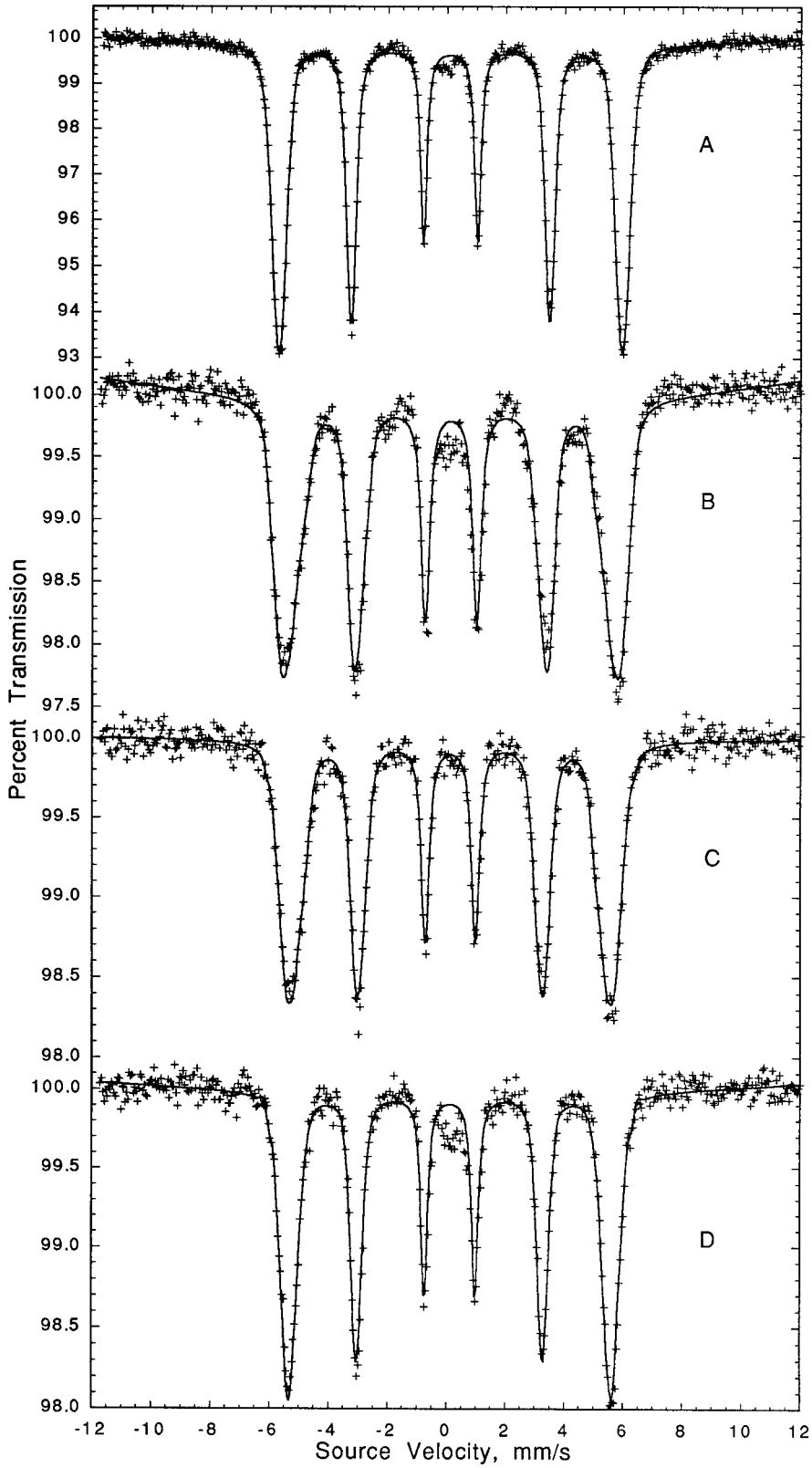

Figure 12. Mössbauer spectra of $Fe_{88}Co_{12}$, A, $Fe_{57}Ni_{43}$, B, $Fe_{33}Co_{32}Ni_{35}$, C, and $Fe_{25}Co_{61}Ni_{14}$, D, obtained at 78 K.

the isomer shift, a correlation which is not taken into account in the distribution fit. In all cases, it was found that there was at most a negligible improvement in the distribution fits if x in the sextet component line ratio of 3:x:1:1:x:3 was allowed to vary from the value of 2 expected for a random powder absorber with no texture. Hence, x was constrained to be 2 for all the fits reported herein.

The iron-57 magnetic hyperfine fields have been measured[45] in the Fe−Co and Fe−Ni alloys, and their compositional dependencies follow a Slater−Pauling curve[46] in a fashion similar to the compositional depen-

(45) Johnson, C. E.; Ridout, M. S.; Cranshaw, T. E.; Madsen, P. E. *Phys. Rev. Lett.* **1961**, *6*, 450.

(46) Kittel, C. *Introduction to Solid State Physics*; Wiley: New York, 1971.

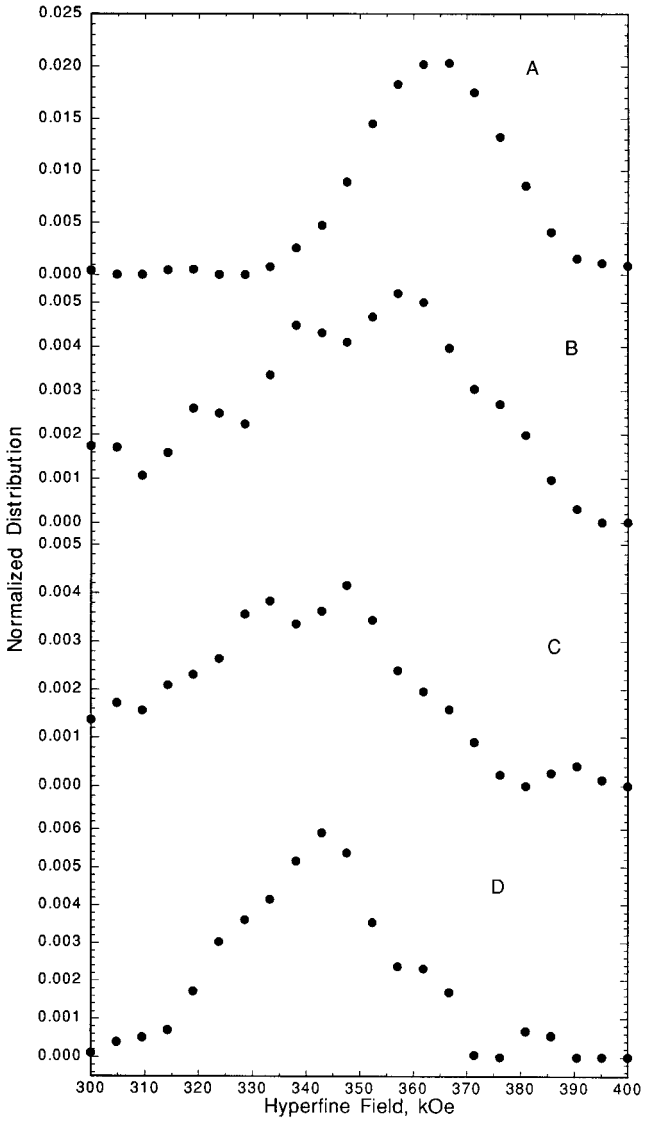

Figure 13. Distribution of the hyperfine fields as determined from the Mössbauer spectra shown in Figure 12.

Table 4. Mössbauer Spectral Parameters for the Alloys

compound	T (K)	δ, mm/s[a]	$\langle H \rangle$ kOe	Γ, mm/s
Fe_{100}	295	0.001	331	0.28
	78	0.111	340	0.25
$Fe_{88}Co_{12}$	295	0.020	358	0.25
	78	0.131	367	0.24
$Fe_{57}Ni_{43}$	295	0.032	316	0.28
	78	0.150	347	0.30
$Fe_{33}Co_{32}Ni_{35}$	295	0.022	325	0.26
	78	0.143	338	0.28
$Fe_{25}Co_{61}Ni_{14}$	295	0.031	336	0.28
	78	0.143	341	0.25

[a] The isomer shifts are reported relative to room temperature α-iron foil.

dence of the magnetic moment in various alloys. These earlier 295 K measurements are plotted in Figure 14, as open squares for the Fe−Co alloys and open circles for the Fe−Ni alloys. The average 295 K hyperfine fields given in Table 4 for the five samples studied herein are also plotted as solid symbols in Figure 14.

The maximum hyperfine field observed at 6.3 d electrons per atom in the Fe−Co alloys may be understood[47] in terms of the changes occurring in the density of states of α-iron as cobalt is introduced into the alloy.

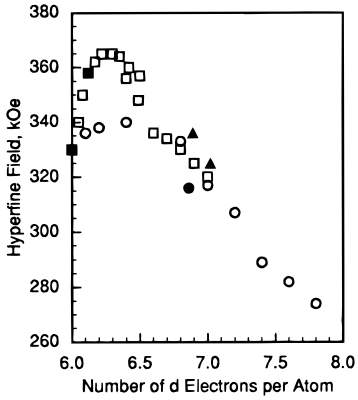

Figure 14. Previously reported[45] hyperfine fields plotted as a function of the number of *d* electrons per atom in the Fe−Co, open squares, and Fe−Ni, open circles, alloys. The 295 K hyperfine fields obtained herein are given for Fe_{100} and $Fe_{88}Co_{12}$ (■), $Fe_{57}Ni_{43}$, (●), and $Fe_{25}Co_{61}Ni_{14}$ and $Fe_{33}Co_{32}Ni_{35}$ (▲).

In α-iron, the Fermi level crosses the spin-up, $t_{2g}e_g$, antibonding band at ca. 0.1 eV below the overlap region of the spin-up and spin-down, $t_{2g}e_g$, antibonding bands. As small amounts of cobalt are added to iron, the additional electrons fill the spin-up band, thus increasing the magnetic moment and the iron hyperfine field, until the Fermi level reaches the overlap region. For higher cobalt concentrations, the additional electrons begin to fill the spin-down band, thus decreasing the magnetic moment and the iron hyperfine field. The maximum observed at 6.3 d electrons per atom in Figure 14 is directly related to a maximum at 6.35 d electrons per atom in the compositional dependence[48] of the electronic specific heat of the bcc iron alloys. Neutron diffraction measurements[49] on Fe−Co and Fe−Ni alloys indicate that the cobalt and nickel magnetic moments are essentially independent of the composition of the alloy, whereas the iron magnetic moment increases up to 3 or 2.5 μ_B for alloys containing 50% added cobalt or nickel, respectively. If the compositional dependencies of the iron magnetic hyperfine fields and the average magnetic moments in the Fe−Co and Fe−Ni alloys are similar, the usual proportionality of ca. 150 kOe/μ_B between these two quantities is, at best, approximate. Actually, the measured magnetic moments would lead to substantially higher fields than those observed experimentally.

As is shown in Figure 14, the average 295 K hyperfine field in $Fe_{88}Co_{12}$, is found exactly on the Slater−Pauling curve obtained for the bulk Fe−Co alloys. As indicated by the X-ray diffraction pattern shown in Figure 9a, $Fe_{88}Co_{12}$ crystallizes in the bcc structure; however, considering its preparation, it is expected to be disordered. This disorder does not seem to affect the magnetic interactions in this nanosize alloy as compared with the bulk alloy.

The hyperfine field observed for $Fe_{57}Ni_{43}$ in Figure 14 lies somewhat below the Slater−Pauling curve observed for the Fe−Ni alloys. This lower than expected hyperfine field may arise from either a mixture of

(47) Goodenough, J. B. *Magnetism and the Chemical Bond;* Wiley: New York, 1963; p 306.
(48) Starke, E. A.; Cheng, C. H.; Beck, P. A. *Phys. Rev.* **1962**, *126*, 1746.
(49) Collins, M. F.; Forsyth, J. B. *Philos. Mag.* **1963**, *8*, 401.

crystalline phases in the sample or extensive disorder due to the preparative method.

The two hyperfine fields in the Fe−Co−Ni alloys (see Figure 14) lie slightly above the Slater-Pauling curve for the Fe−Co alloys. A similar observation was reported by Achilleos et al.,[50] who measured the average magnetic moments of various ternary Fe−Co−Ni alloys in the compositional range investigated herein. They attributed the higher fields in the Fe−Co−Ni alloys to magnetic interactions stronger in Fe−Co than those in Fe−Ni.

The increase in the isomer shifts observed upon alloying iron with cobalt or nickel (see Table 4) is in agreement with the trend observed[51] in the Fe−Co alloys, i.e., an increase in isomer shift up to 25 atom % of cobalt in iron and then a decrease for higher cobalt concentrations. The increase in isomer shift at low cobalt concentration is the result of a decrease in the 4*s* electron density, a decrease which may be concomitant with the filling of the 3d band. The Fe−Ni alloys are known to have isomer shifts at 295 K which are slightly positive relative to α-iron, i.e., kamacite, the bcc α-Fe−Ni alloy, has an isomer shift[52] of ca. 0.02 mm/s, and γ−$Fe_{20}Ni_{80}$ has an isomer shift[53] of 0.044 mm/s. The value of 0.032 mm/s measured herein for $Fe_{57}Ni_{43}$ is in this range.

It is interesting to compare the hyperfine fields observed for $Fe_{57}Ni_{43}$ in Table 4 with those measured[52,53] for kamacite, the α-Fe−Ni alloys, and γ−$Fe_{20}Ni_{80}$. At 78 K, the fields in $Fe_{57}Ni_{43}$ and kamacite are identical at 347 kOe. However, at 295 K, the field in $Fe_{57}Ni_{43}$ is 20 kOe smaller than that in kamacite. In contrast, the 347 kOe field in $Fe_{57}Ni_{43}$ is substantially larger than the 295 K field of 250 kOe observed[53] in γ−$Fe_{20}Ni_{80}$ but is very similar to the field of 310 kOe observed in a typical fcc Fe−Ni alloy containing 35−50% nickel. These differences may be the result of a mixture of α-phases and γ-phases in the $Fe_{57}Ni_{43}$ sample, a mixture which is evident in the X-ray diffraction pattern shown in Figure 8b.

Finally, it is worth noting the differences between the sonochemically prepared,[54] nanosized, amorphous Fe−Ni alloys and the Fe−Ni and Fe−Co alloys studied herein. The sonochemically prepared Fe−Ni alloys are amorphous just like the amorphous iron sample previously studied[55] by Mössbauer spectroscopy. They consist of small 6 nm diameter magnetic particles, particles which are superparamagnetic at room temperature and hence do not show the typical magnetic sextet Mössbauer spectra shown in Figure 12. In contrast, the Fe−Ni alloys prepared by the electropulse method consist of larger ca. 100 nm diameter particles, particles which show crystallinity and long-range magnetic order as is indicated by the magnetic sextet Mössbauer spectra shown in Figure 12.

Conclusions

The most interesting aspect of this work is the production of very fine particles with a rather simple and inexpensive method. Their composition and homogeneity are easily controlled by selecting the electrochemical and ultrasound parameters. The X-ray diffraction patterns indicate the following: first, in the Co−Ni system, only the high-temperature fcc solid solutions are produced; second, in the Fe−Ni system, solid solutions with ranges of composition larger than those of the thermodynamic ranges are produced; third, in the Fe−Co system for high iron concentration, the bcc phase is produced; and fourth, in the Fe−Co−Ni system at high iron and nickel concentration, the bcc iron and fcc nickel phases, respectively, are produced. The Mössbauer spectral results indicate that the magnetic properties of the alloys prepared by the electropulse method closely resemble those of the bulk alloys.

Acknowledgment. J.L.D. is indebted to the National Fund for Scientific Research of Belgium for financial support. Part of this research was also supported by the U.S. National Science Foundation through a Division of Materials Research Grant No. 95-21739.

CM990461N

(50) Achilleos, C. A.; Kyprianidis, I. M.; Tsoukalas, I. A. *Solid State Commun.* **1991**, *79*, 209.
(51) De Mayo, B.; Forester, D. W.; Spooner, S. *J. Appl. Phys.* **1970**, *41*, 1319.
(52) Grandjean, F.; Long, G. J.; Hautot, D.; Whitney, D. L. *Hyperfine Interact.* **1998**, *116*, 105.
(53) Scorzelli, R. B.; Galvao da Silva, E.; Kaito, C.; Saito, Y.; McElfresh, M.; Elmassalami, M. *Hyperfine Interact.* **1994**, *94*, 2337.
(54) Shafi, K. V. P. M.; Gedanken, A.; Goldfarb, R. B.; Felner, I. *J. Appl. Phys.* **1997**, *81*, 6901.
(55) Long, G. J.; Hautot, D.; Pankhurst, Q. A.; Vandormael, D.; Grandjean, F.; Gaspard, J. P.; Briois, V.; Hyeon, T.; Suslick, K. S. *Phys. Rev. B* **1998**, *57*, 10 716.